

Article

# Wideband Ge-Rich SiGe Polarization-Insensitive Waveguides for Mid-Infrared Free-Space Communications

Vladyslav Vakarin <sup>1,\*</sup>, Joan Manel Ramírez <sup>1</sup>, Jacopo Frigerio <sup>2</sup>, Qiankun Liu <sup>1</sup>, Andrea Ballabio <sup>2</sup> , Xavier Le Roux <sup>1</sup>, Carlos Alonso-Ramos <sup>1</sup>, Giovanni Isella <sup>2</sup>, Pavel Cheben <sup>3</sup>, Winnie N. Ye <sup>4</sup>, Laurent Vivien <sup>1</sup> and Delphine Marris-Morini <sup>1</sup>

<sup>1</sup> Centre de Nanosciences et de Nanotechnologies (C2N), Université Paris Saclay, Université Paris Sud, CNRS, 91405 Orsay, France; joan-manel.ramirez@u-psud.fr (J.M.R.); qiankun.liu@u-psud.fr (Q.L.); xavier.leroux@u-psud.fr (X.L.R.); carlos.ramos@u-psud.fr (C.A.-R.); laurent.vivien@u-psud.fr (L.V.); delphine.morini@u-psud.fr (D.M.-M.)

<sup>2</sup> L-NESS, Dipartimento di Fisica del Politecnico di Milano, Polo di Como, Via Anzani 42, I 22100 Como, Italy; jacopo.frigerio84@gmail.com (J.F.); andrea.ballabio@polimi.it (A.B.); giovanni.isella@polimi.it (G.I.)

<sup>3</sup> National Research Council, Ottawa, ON K1A 0R6, Canada; pavel.cheben@nrc-cnrc.gc.ca

<sup>4</sup> Department of Electronics, Carleton University, 1125 Colonel by Dr., Ottawa, ON K1S 5B6, Canada; WinnieYe@cunet.carleton.ca

\* Correspondence: vevakarin@gmail.com

Received: 19 June 2018; Accepted: 12 July 2018; Published: 16 July 2018



**Featured Application:** mid-infrared free-space communications.

**Abstract:** The recent development of quantum cascade lasers, with room-temperature emission in the mid-infrared range, opened new opportunities for the implementation of ultra-wideband communication systems. Specifically, the mid-infrared atmospheric transparency windows, comprising wavelengths between 3–5  $\mu\text{m}$  and 8–14  $\mu\text{m}$ , have great potential for free-space communications, as they provide a wide unregulated spectrum with low Mie and Rayleigh scattering and reduced background noise. Despite the great efforts devoted to the development of mid-infrared sources and detectors, little attention is dedicated to the management of polarization for signal processing. In this work, we used Ge-rich SiGe alloys to build a wideband and polarization-insensitive mid-infrared photonic platform. We showed that the gradual index change in the SiGe alloys enabled the design of waveguides with remarkably low birefringence, below  $2 \times 10^{-4}$ , over ultra-wide wavelength ranges within both atmospheric transparency windows, near wavelengths of 3.5  $\mu\text{m}$  and 9  $\mu\text{m}$ . We also report on the design of a polarization-independent multimode interference device achieving efficient power splitting in an unprecedented 4.5- $\mu\text{m}$  bandwidth at around 10- $\mu\text{m}$  wavelength. The ultra-wideband polarization-insensitive building blocks presented here pave the way for the development of high-performance on-chip photonic circuits for next-generation mid-infrared free-space communication systems.

**Keywords:** photonic integrated circuits; mid-infrared; polarization-insensitive

## 1. Introduction

The mid-infrared (MIDIR) spectral region (2–20  $\mu\text{m}$ ) became a field of major applicative interest over the past decade. Sharp and strong molecular absorption bands of various chemical compounds in that region make the use of MIDIR radiation well-adapted for a large number of applications, including biosensing and medical diagnosis [1–3], security and defense [4–7], and astronomy, among others [8,9]. Such a wide range of applications led to the development of a plethora of photonic components, including sources [10–12], waveguides, spectrometers [13,14], and modulators for

lock-in detection [15,16]. Moreover, in order to reach higher MIDIR wavelengths, various photonic platforms were developed, such as III-V materials [17–19], chalcogenide [20–23], and silicon and silicon-compatible materials [24–40]. MIDIR photonic integrated circuits leveraging the mature Si technology have great potential for low-power consumption and low-cost systems that are meant to outperform existing technologies. Among the available group IV-compatible MIDIR platforms, silicon germanium (SiGe), and more specifically, Ge-rich SiGe alloys exhibit a compelling combination of flexible material tunability [34], large transparency, wideband operation [35–37], and remarkable nonlinear properties [40]. Here, we study the use of the Ge-rich SiGe platform to develop wideband and polarization-independent MIDIR components for free-space communications.

Earth atmosphere's absorption spectrum contains two transparency windows in the MIDIR region that are very interesting for free-space communications. These two MIDIR windows, which lie within the 3–5  $\mu\text{m}$  (mid-wavelength IR, MWIR) and 8–14  $\mu\text{m}$  (long-wavelength IR, LWIR) wavelength ranges, present two major advantages compared to their near-infrared (NIR) counterparts, namely (i) reduced Rayleigh and Mie scattering [41,42], and (ii) improved robustness against spectral radiance from the main sources of background noise in free-space optical communications (moon, sun, earth, and city lights) [41,42]. As light arrives at the receiver point with an unknown polarization state [43,44], we propose the development of polarization-insensitive photonic circuits for information processing. Main geometric parameters of Ge-rich SiGe waveguides were optimized to yield wideband polarization-independent behavior within both atmospheric transparency windows. The difference between the effective indexes of the fundamental transverse electric (TE) mode and the fundamental transverse magnetic (TM) mode was kept below  $2 \times 10^{-4}$ , which enabled the implementation of polarization-insensitive devices and circuits. Moreover, this wideband operation allows, for example, transmitting a large number of communication channels, each carrying information from a directly modulated MIDIR quantum cascade laser (QCL) [45]. In addition, a wideband and polarization-insensitive Ge-rich SiGe multimode interference structure (MMI) was optimized to operate in the second atmospheric transparency window. The operational  $-1$  dB bandwidth for the designed MMI extends across a wavelength of 7.5  $\mu\text{m}$  to 12.65  $\mu\text{m}$ . These basic building blocks pave the way for the development of polarization-insensitive MIDIR photonic components in on-chip transceivers for free-space communications.

## 2. Materials and Methods

A commercial-grade simulator eigenmode solver and propagator was used to perform calculations for the waveguide and MMI study [46]. The refractive index of the SiGe alloy was obtained via linear interpolation of the index with respect to germanium concentration ( $x$ ) in the alloy, as described by Equation (1), where  $n_{\text{Si}}$  and  $n_{\text{Ge}}$  are the respective refractive indexes of Si and Ge.

$$n_{\text{Si}_{1-x}\text{Ge}_x} = n_{\text{Si}}(1 - x) + xn_{\text{Ge}}. \quad (1)$$

For the simulation, experimental values of the Ge refractive index were used [47]. As the simulations were performed over a wide range of wavelengths, the refractive-index dispersion was taken into account for the Ge-rich SiGe waveguides. As an example, the refractive-index evolution of the  $\text{Si}_{0.2}\text{Ge}_{0.8}$  alloy is shown in Figure 1. For instance, at a wavelength of 3  $\mu\text{m}$ ,  $n_{\text{Si}} = 3.43$  and  $n_{\text{Ge}} = 4.04$ . It is worth noting that, for SiGe waveguides, the mode dispersion dominates over the material refractive-index dispersion in the MIDIR [34]. Consequently, the mode-dispersion engineering approach by means of geometric parameter optimization was chosen to obtain the polarization-insensitive and wideband integrated photonic components.

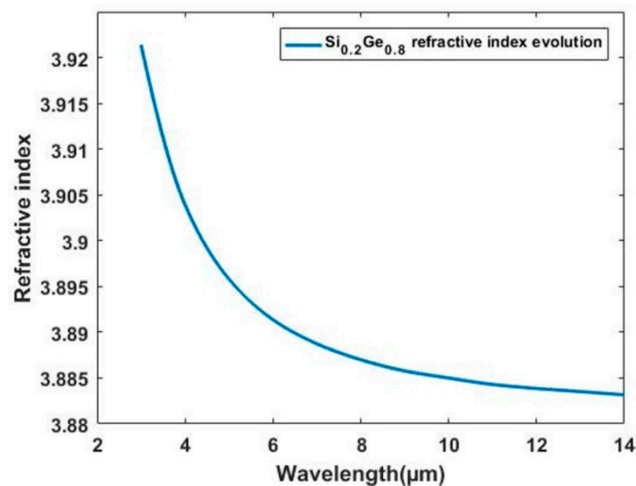


**Figure 1.** Refractive index evolution of the  $\text{Si}_{0.2}\text{Ge}_{0.8}$  alloy in the mid-infrared (MIDIR) spectral region.

### 3. Results

#### 3.1. Wideband Polarization-Insensitive Waveguides

For the implementation of polarization-insensitive Ge-rich SiGe waveguides, the following epitaxial configuration was chosen (Figure 2a): 2  $\mu\text{m}$  of constant  $\text{Si}_{0.2}\text{Ge}_{0.8}$  on an 11- $\mu\text{m}$ -thick SiGe graded buffer layer (GB), where the germanium concentration increased linearly in the vertical direction until the terminal composition of  $\text{Si}_{0.21}\text{Ge}_{0.79}$ . The GB provides three major advantageous features: (i) it guarantees a good material quality through the accommodation of a gradual lattice [48], (ii) it isolates the optical mode from the silicon-rich region and the silicon substrate, avoiding loss via multi-phonon absorption at wavelengths higher than 7  $\mu\text{m}$  [49], and (iii) it allows broadband and low-loss operation by means of combining low MIDIR material dispersion in Si and Ge, and the mode size self-adaptation effect [34,35]. Noticeably, low propagation losses and a wideband Mach Zehnder interferometer (MZI) operation were previously demonstrated based on this epitaxial layer [35,36]. The inspected wavelength was limited by the available spectral range in our experimental set-up, which covered the wavelengths between 5  $\mu\text{m}$  and 8.5  $\mu\text{m}$ . Flat low-loss conditions were obtained for both TE and TM polarizations. On the basis of the above features, such an epitaxial layer is a promising candidate for achieving a polarization-insensitive waveguide targeting both MIDIR atmospheric transparency windows with a single-material platform. However, despite all the above-mentioned works on SiGe platforms, polarization sensitivity is yet to be evaluated, and consequently, became the main subject of interest in the presented work.

Firstly, the waveguide geometry was optimized to achieve polarization-independent behavior in the MWIR range. The waveguide birefringence, i.e., the difference between effective mode indexes for TE ( $n_{\text{eff,TE}}$ ) and TM ( $n_{\text{eff,TM}}$ ) polarizations ( $|n_{\text{eff,TE}} - n_{\text{eff,TM}}|$ ), was studied as a function of the width ( $W$ ) and etching depth ( $D$ ) for 10 different wavelengths between 3  $\mu\text{m}$  and 5  $\mu\text{m}$ . As an example, the maps for the wavelengths of 3.5  $\mu\text{m}$ , 4  $\mu\text{m}$ , and 5  $\mu\text{m}$  are shown in Figure 2b–d, respectively. These maps clearly illustrate the wavelength dependence of the birefringence, and give insight into the zone where polarization-insensitive geometries can be localized. One can observe the evolution of the zero-birefringence line as a function of the wavelength. When the wavelength increases, the zero-birefringence line shifts toward wider and deeper-etched waveguide geometries.

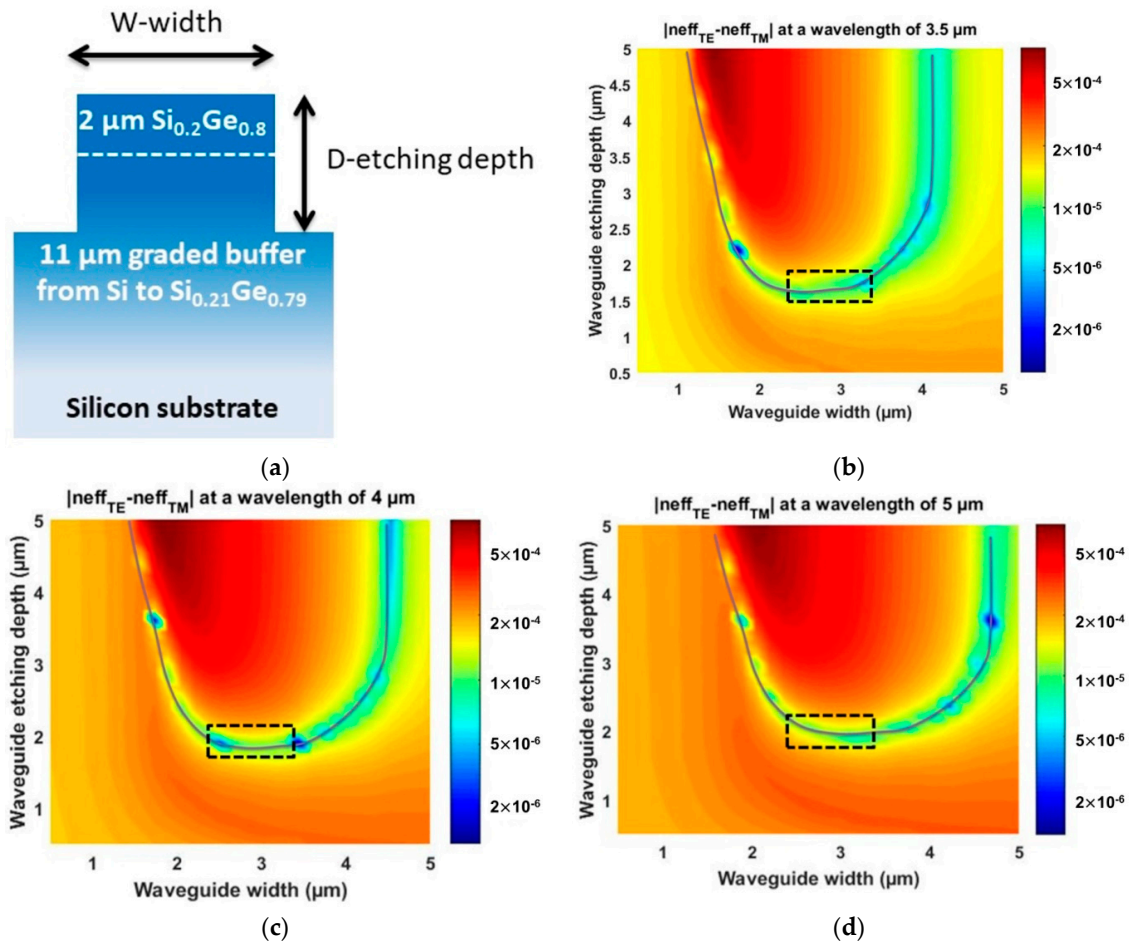


**Figure 2.** (a) Schematic view of the waveguide cross-section. Depending on the design, the etching depth ( $D$ ) can stop in the graded buffer layer, or in the  $\text{Si}_{0.2}\text{Ge}_{0.8}$  top layer. Birefringence evolution as a function of waveguide dimensions for wavelengths of (b)  $3.5\ \mu\text{m}$ , (c)  $4\ \mu\text{m}$ , and (d)  $5\ \mu\text{m}$ . In (b–d), the gray line represents the zero-birefringence line, i.e., no difference between effective mode indexes for transverse electric (TE;  $n_{\text{eff}_{\text{TE}}}$ ) and transverse magnetic (TM;  $n_{\text{eff}_{\text{TM}}}$ ) polarizations,  $|n_{\text{eff}_{\text{TE}}} - n_{\text{eff}_{\text{TM}}}| = 0$ . The black dashed rectangle corresponds to a set of dimensions where low birefringence was obtained for the various wavelengths.

Remarkably, the bottom zone including the zero-birefringence line (black dashed rectangle in Figure 2b–d) kept low birefringence values despite the wavelength change. Hence, wideband polarization-insensitive waveguide configurations were expected to be localized in this region.

In order to finely optimize waveguide dimensions for broadband polarization-insensitive operation, we studied the birefringence variation as a function of the wavelength. Firstly, we defined the beating length  $L_{\pi}$  as

$$L_{\pi} = \frac{\lambda}{2|n_{\text{eff}_{\text{TE}}} - n_{\text{eff}_{\text{TM}}}|} \tag{2}$$

At a given wavelength, the polarization-insensitive waveguide maximizes the  $L_{\pi}$  value. However, if a broadband polarization-insensitive operation is envisioned, maximizing  $L_{\pi}$  at a given wavelength is not sufficient. Hence, we defined the following figure of merit:

$$L_{\text{geom}} = \left( \prod_{i=1}^N L_{\pi_i} \right)^{\frac{1}{N}}, \tag{3}$$

where  $L_{geom}$  is the geometric mean value of  $L_{\pi}$  over  $N$  different wavelengths. The waveguide geometry was optimized to maximize  $L_{geom}$ , thus minimizing the birefringence over the selected spectral range. Figure 3a shows  $L_{geom}$  as a function of waveguide width ( $W$ ) and etching depth ( $D$ ), calculated for 10 wavelengths within the MWIR range. As expected from the birefringence maps shown in Figure 2,  $L_{geom}$  was maximized in the bottom zone close to the zero-birefringence line (black dashed rectangle).  $L_{geom}$  was also maximized in the zone comprising waveguides with widths between  $4 \mu\text{m}$  and  $5 \mu\text{m}$ , and etching depths between  $2.5 \mu\text{m}$  and  $5 \mu\text{m}$ . However, these waveguides are highly multimode, which is not desirable for the implementation of complex circuits. Therefore, we chose  $W = 3.4 \mu\text{m}$  and  $D = 1.9 \mu\text{m}$  as the optimal design. The field-intensity profiles for the optimized waveguide geometry are depicted in Figure 3b,c for TE and TM modes, respectively. As can be observed, similar mode profiles and confinements were obtained for both polarizations. Figure 3d shows the birefringence as a function of the wavelength for the optimized waveguide. Interestingly, the proposed design ensured birefringence below  $2 \times 10^{-4}$  across wavelengths of  $3 \mu\text{m}$  and  $4.8 \mu\text{m}$ , almost entirely covering the atmospheric transparency MWIR window. In other words, the TE and TM modes were  $\pi$ -shifted only after a propagation distance of  $1.2 \text{ cm}$  at a wavelength of  $4.8 \mu\text{m}$ .

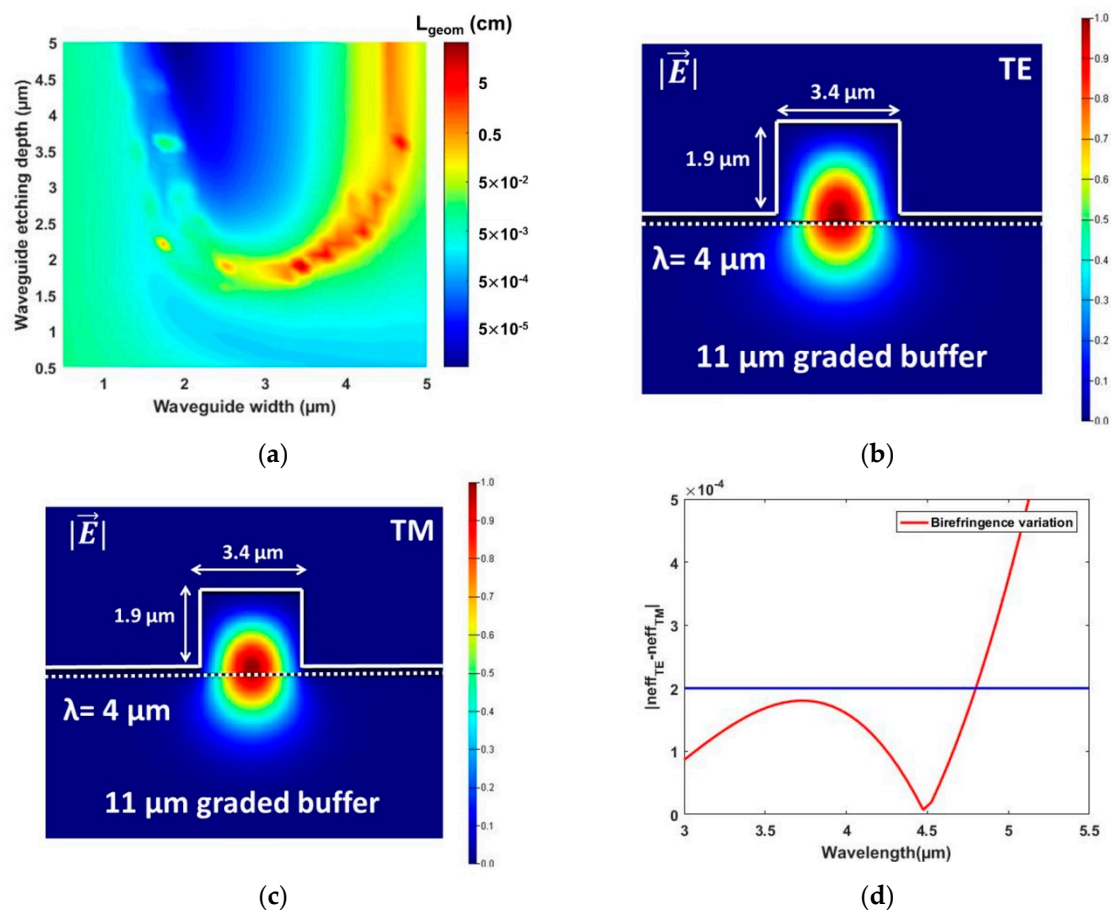


**Figure 3.** (a)  $L_{geom}$  ( $L_{\pi}$  geometric mean value calculated over 10 different wavelengths) as a function of the waveguide dimensions; the  $L_{\pi}$  values are given in cm. Waveguide geometries optimized for mid-wavelength IR (MWIR) and field-intensity profiles for (b) TE polarization and (c) TM polarization at a  $4\text{-}\mu\text{m}$  wavelength. The white dotted line delimits the frontier between the graded buffer and the constant composition layer. The shown field profiles are cropped zoomed images from the bigger simulation window. (d) Birefringence evolution as a function of the wavelength for the optimized cross-section. The blue line marks the chosen limit for the birefringence at  $\Delta n_{eff} = 2 \times 10^{-4}$ .

A similar approach was used to design the wideband polarization-insensitive waveguide in the LWIR. The optimized dimensions and the TE-mode field-intensity profile are presented in Figure 4a; the waveguide was 5.4 μm wide with a 3.1-μm etching depth. Its birefringence, which is shown in Figure 4b, was below  $2 \times 10^{-4}$  across the wavelengths spanning 8.22 μm to 10.36 μm (i.e., a polarization-insensitive bandwidth larger than 2 μm). These low birefringence values correspond to  $L_{\pi}$  values higher than 2.5 cm on the full operational wavelength range.

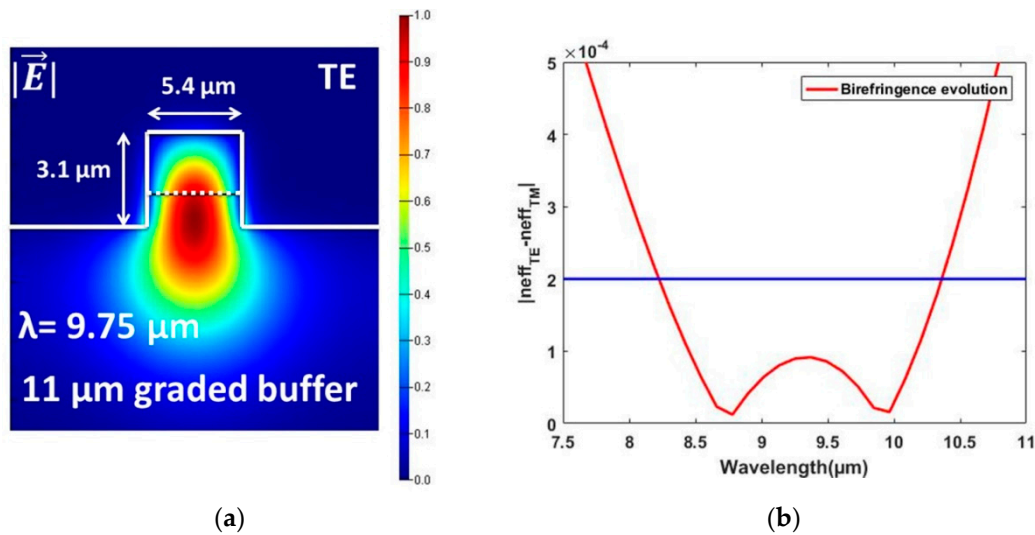


**Figure 4.** (a) The waveguide geometry optimized for long-wavelength IR (LWIR), and the field-intensity profile for TE polarization at a wavelength of 9.75 μm. The field-intensity profile is a cropped zoomed image from the bigger simulation window. The white dotted line delimits the frontier between the graded buffer and the constant composition layer. (b) Birefringence evolution as a function of the wavelength for the optimized cross-section. The blue line marks the chosen limit for the birefringence at  $\Delta n_{\text{eff}} = 2 \times 10^{-4}$ .

### 3.2. Wideband Polarization-Insensitive MMI

Following the optimization of the waveguide cross-section for wideband polarization-insensitive operation, a wideband polarization-insensitive MMI was designed in the MIDIR LWIR range. The MMI was designed according to the principles exposed in References [50,51]. To design such a device, it was necessary to introduce the MMI beating length ( $L_{\pi_{\text{MMI}}}$ ), defined as

$$L_{\pi_{\text{MMI}}} = \frac{\lambda}{2|n_{\text{eff,mode 1}} - n_{\text{eff,mode 2}}|}, \quad (4)$$

where the mode effective indexes correspond to the lowest-order modes in the multimode region for a given polarization. The length of the  $1 \times 2$  MMI is related to the beat length by  $\frac{3}{8}L_{\pi_{\text{MMI}}}$  [50]. To design an MMI operating for both polarizations in a wideband range, it is important to consider the evolution of  $\frac{3}{8}L_{\pi_{\text{MMI}}}$  for both TE and TM polarizations. More specifically, Figure 5a shows the influence of the MMI width on the difference between optimal MMI lengths for TE and TM as a function of the wavelength. The etching depth was chosen as 3.1 μm, as it was shown to provide a polarization-insensitive waveguide in the LWIR range. Figure 5a shows that the difference between MMI lengths in TE and TM polarizations was minimized to a width of 20 μm in the spectral range between 7.5 and 13 μm. Increasing MMI width resulted in an increase in the difference between TE and TM MMI optimal lengths. For a width of 20 μm, at a wavelength of 13 μm in TE polarization, the MMI contains three modes which is the limit for obtaining MMI behavior.

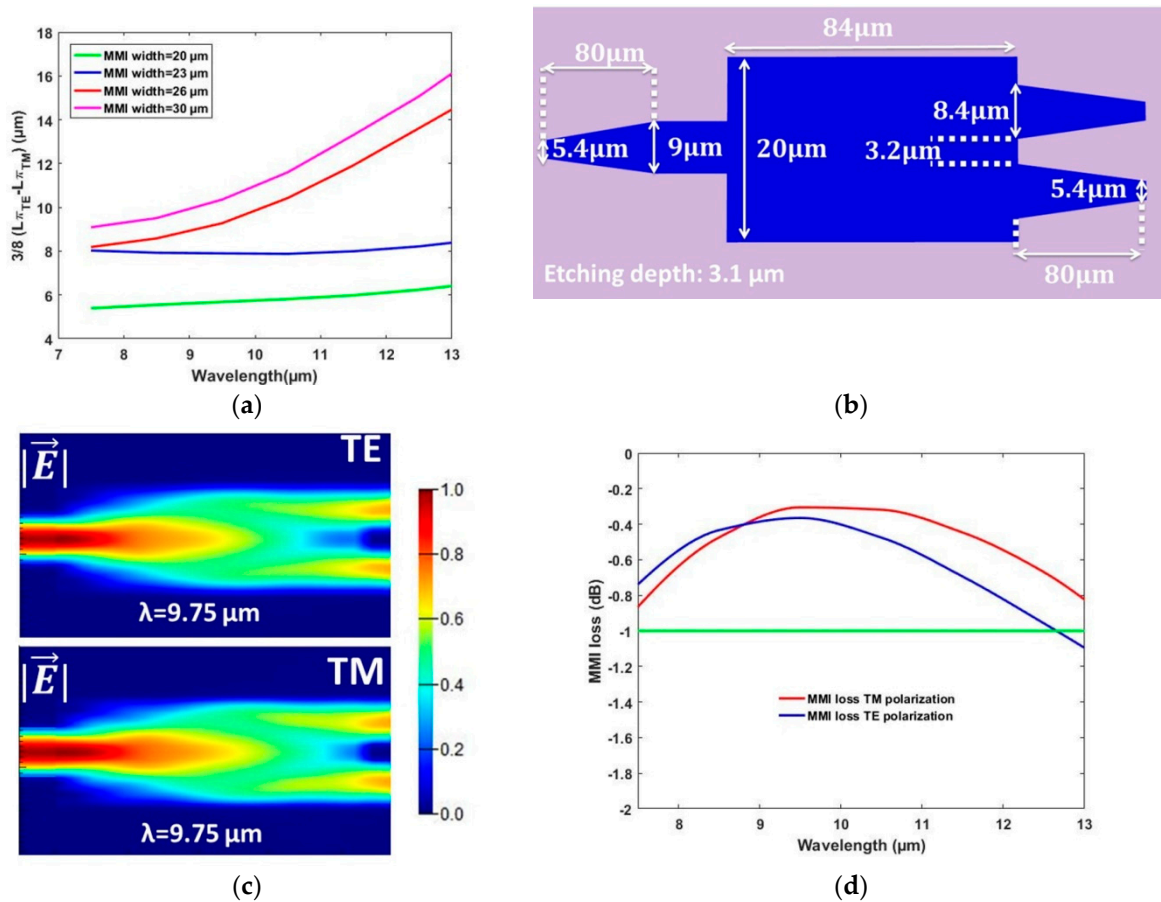


**Figure 5.** (a) Evolution of  $\frac{3}{8}L_{\pi_{MMI}}$  (multimode interference structure (MMI) beating length) for TE and TM polarization as function of wavelength and MMI width. (b) Schematic view of the optimized MMI. (c) Field-intensity profile for the optimized structure for TE polarization (top) and TM polarization (bottom). (d) MMI loss as a function of the wavelength for TE and TM polarizations.

The optimized MMI design is presented in Figure 5b, whereby a 20- $\mu\text{m}$ -wide and 84- $\mu\text{m}$ -long MMI was chosen with input and output tapering of 80  $\mu\text{m}$  to avoid any bandwidth limitation from the tapers. The optimized MMI structure induces a phase shift between TE and TM modes of  $3.9^\circ$  at the output of the MMI at a wavelength of 9.75  $\mu\text{m}$  (i.e., more than 40 MMIs are needed to realize a  $\pi$ -shift between the TE and TM modes). The field-intensity profiles extracted from the propagation simulations in TE and TM polarizations are shown in Figure 5c. Both polarizations exhibited similar propagation profiles. Moreover, as shown in Figure 5d, TE and TM polarizations yielded very similar performances, with losses lower than 1 dB in the 7.5  $\mu\text{m}$  to 12.65  $\mu\text{m}$  and 7.5  $\mu\text{m}$  to 13  $\mu\text{m}$  wavelength ranges for TE and TM polarizations, respectively. Consequently, the MIDIR LWIR transparency window is successfully covered with a single MMI device.

#### 4. Discussion

The performance of the proposed Ge-rich SiGe polarization-insensitive building blocks could be evaluated in terms of the number of channels that each structure can cover. It is important to point out that, regardless of polarization insensitivity, another key parameter is the broadband operation of the presented devices. As an example, if we consider a channel width of 5 nm, which can contain a QCL laser line with a maximum width of  $0.2 \text{ cm}^{-1}$ , we would be able to allocate more than 300 channels in each MIDIR atmosphere transparency window with the optimized waveguide presented here (Table 1).

**Table 1.** Optimized Ge-rich SiGe structures and the number of 5-nm channels that can be covered.

MIDIR <sup>1</sup> Transparency Window	Component	Dimensions	Number of Channels
MWIR <sup>2</sup>	waveguide	3.4 $\mu\text{m}$ width $\times$ 1.9 $\mu\text{m}$ etching depth	360
LWIR <sup>3</sup>	waveguide	5.4 $\mu\text{m}$ width $\times$ 3.1 $\mu\text{m}$ etching depth	428

<sup>1</sup> MIDIR: mid infrared, <sup>2</sup> MWIR window: mid-wavelength infrared window,  $\lambda = 3\text{--}5 \mu\text{m}$ , <sup>3</sup> LWIR window: long-wavelength infrared window,  $\lambda = 8\text{--}14 \mu\text{m}$ .

The polarization-independent wideband components reported in this work are a first step toward the development of integrated polarization-insensitive and broadband Ge-rich SiGe photonic circuits for MIDIR free-space communications. For instance, the polarization-insensitive wideband MMI, and by extension, the Mach Zehnder interferometer can be employed to implement building blocks such as Fourier-transform spectrometers [13], multiplexers and demultiplexers [52], switches, and more.

In conclusion, the use of broadband components paves the way for the reduction of needed components and the number of building blocks in general, which consequently results in efficient and cost-effective ground–ground, satellite–ground, and satellite–satellite free-space communications in the MIDIR range.

**Author Contributions:** Data curation, V.V., J.M.R. Formal analysis, V.V., J.F., and A.B. Funding acquisition, W.N.Y., G.I. and D.M.-M. Investigation, V.V., J.M.R. and C.A.-R. Supervision, P.C., W.N.Y., and D.M.-M. Validation, V.V., L.V., X.L.R. Writing—original draft, V.V., J.M.R., and Q.L. Writing—review and editing, C.A.-R., G.I., and D.M.-M.

**Funding:** The European Research Council (ERC) under the European Union’s Horizon 2020 research and innovation program (No. 639107-INSPIRE).

**Conflicts of Interest:** The authors declare no conflict of interest.

## References

1. Sieger, M.; Mizaikoff, B. Toward on-chip mid-infrared sensors. *Anal. Chem.* **2016**, *88*, 5562–5573. [[CrossRef](#)] [[PubMed](#)]
2. Yu, M.C.; Rich, P.; Foreman, L.; Smith, J.; Yu, M.S.; Tanna, A.; Dibbur, V.; Unwin, R.; Tam, F.W. Label Free Detection of Sensitive Mid-Infrared Biomarkers of Glomerulonephritis in Urin using Fourier Transform Spectroscopy. *Sci. Rep.* **2017**, *7*, 4601. [[CrossRef](#)] [[PubMed](#)]
3. Etezadi, D.; Warner, J.B., IV; Ruggeri, F.S.; Dietler, G.; Lashuel, H.A.; Altug, H. Nanoplasmonic mid-infrared biosensor for in vitro protein secondary structure detection. *Light Sci. Appl.* **2017**, *6*, e17029. [[CrossRef](#)]
4. Chang, Y.C.; Wägli, P.; Paeder, V.; Homsy, A.; Hvozdar, L.; van der Wal, P.; Di Francesco, J.; de Rooji, N.F.; Herzig, H.P. Cocaine detection by a mid-infrared waveguide integrated with a microfluidic chip. *Lab Chip* **2012**, *12*, 3020–3023. [[CrossRef](#)] [[PubMed](#)]
5. Bauer, C.; Willer, U.; Lewicki, R.; Pohlkötter, A.; Kosterev, A.; Kosynkin, D.; Tittel, F.K.; Schade, W. A Mid-infrared QEPAS sensor device for TATP detection. *J. Phys. Conf. Ser.* **2009**, *157*, 012002. [[CrossRef](#)]
6. Herbst, J.; Hildenbrand, J.; Wöllenstein, J.; Lambrecht, A. TATP and TNT detection by mid-infrared transmission spectroscopy. In *Infrared Technology and Applications XXXV*; International Society for Optics and Photonics: Orlando, FL, USA, 2009; Volume 7298, p. 72983W. [[CrossRef](#)]
7. Kornaszewski, Ł.; Gayraud, N.; Stone, J.M.; MacPherson, W.N.; George, A.K.; Knight, J.C.; Hand, D.P.; Reid, D.T. Mid-infrared methane detection in a photonic bandgap fiber using a broadband optical parametric oscillator. *Opt. Express* **2007**, *15*, 11219–11224. [[CrossRef](#)] [[PubMed](#)]
8. Diener, R.; Tepper, J.; Labadie, L.; Pertsch, T.; Nolte, S.; Minardi, S. Towards 3D-photonic, multi-telescope beam combiners for mid-infrared astrointerferometry. *Opt. Express* **2017**, *25*, 19262–19274. [[CrossRef](#)] [[PubMed](#)]
9. Gross, S.; Jovanovic, N.; Sharp, A.; Ireland, M.; Lawrence, J.; Withford, M.J. Low loss mid-infrared ZBLAN waveguides for future astronomical applications. *Opt. Express* **2015**, *23*, 7946–7956. [[CrossRef](#)] [[PubMed](#)]

10. Nguyen-Van, H.; Baranov, A.N.; Loghmari, Z.; Cerutti, L.; Rodriguez, J.B.; Tournet, J.; Narcy, G.; Boissier, G.; Patriarche, G.; Bahriz, M.; et al. Quantum cascade lasers grown on silicon. *Sci. Rep.* **2018**, *8*, 7206. [[CrossRef](#)] [[PubMed](#)]
11. Bahriz, M.; Lollia, G.; Baranov, A.N.; Teissier, R. High temperature operation of far infrared ( $\lambda \approx 20 \mu\text{m}$ ) InAs/AlSb quantum cascade lasers with dielectric waveguide. *Opt. Express* **2015**, *23*, 1523–1528. [[CrossRef](#)] [[PubMed](#)]
12. Faist, J.; Capasso, F.; Sirtori, C.; Sivco, D.L.; Baillargeon, J.N.; Hutchinson, A.L.; Chu, S.-N.; Cho, A.Y. High power mid-infrared ( $\lambda \sim 5 \mu\text{m}$ ) quantum cascade lasers operating above room temperature. *Appl. Phys. Lett.* **1996**, *68*, 3680–3682. [[CrossRef](#)]
13. Nedeljkovic, M.; Velasco, A.V.; Khokhar, A.Z.; Del age, A.; Cheben, P.; Mashanovich, G.Z. Mid-infrared silicon-on-insulator Fourier-transform spectrometer chip. *IEEE Photonics Technol. Lett.* **2016**, *28*, 528–531. [[CrossRef](#)]
14. Vasiliev, A.; Muneeb, M.; Allaert, J.; Van Campenhout, J.; Baets, R.; Roelkens, G. Integrated Silicon-on-Insulator Spectrometer With Single Pixel Readout for Mid-Infrared Spectroscopy. *IEEE J. Sel. Top. Quantum* **2018**, *24*. [[CrossRef](#)]
15. Chiles, J.; Fathpour, S. Mid-infrared integrated waveguide modulators based on silicon-on-lithium-niobate photonics. *Optica* **2014**, *1*, 350–355. [[CrossRef](#)]
16. Nedeljkovic, M.; Stankovic, S.; Mitchell, C.J.; Khokhar, A.Z.; Reynolds, S.A.; Thomson, D.J.; Gardes, F.Y.; Littlejohns, C.G.; Reed, G.T.; Mashanovich, G.Z. Mid-infrared thermo-optic modulators in Si. *IEEE Photonics Technol. Lett.* **2014**, *26*, 1352–1355. [[CrossRef](#)]
17. Wang, R.; Vasiliev, A.; Muneeb, M.; Malik, A.; Sprengel, S.; Boehm, G.; Amann, M.C.; Symonyte, I.; Vizbaras, K.; Baets, R.; et al. III–V-on-Silicon Photonic Integrated Circuits for Spectroscopic Sensing in the 2–4  $\mu\text{m}$  Wavelength Range. *Sensors* **2017**, *17*, 1788. [[CrossRef](#)] [[PubMed](#)]
18. Roux, S.; Cerutti, L.; Tournie, E.; G erard, B.; Patriarche, G.; Grisard, A.; Lallier, E. Low-loss orientation-patterned GaSb waveguides for mid-infrared parametric conversion. *Opt. Mater. Express* **2017**, *7*, 3011–3016. [[CrossRef](#)]
19. Gilles, C.; Orbe, L.J.; Carpintero, G.; Maisons, G.; Carras, M. Mid-infrared wavelength multiplexer in InGaAs/InP waveguides using a Rowland circle grating. *Opt. Express* **2015**, *23*, 20288–20296. [[CrossRef](#)] [[PubMed](#)]
20. Ma, P.; Choi, D.Y.; Yu, Y.; Gai, X.; Yang, Z.; Debbarma, S.; Madden, S.; Luther-Davies, B. Low-loss chalcogenide waveguides for chemical sensing in the mid-infrared. *Opt. Express* **2013**, *21*, 29927–29937. [[CrossRef](#)] [[PubMed](#)]
21. Han, Z.; Lin, P.; Singh, V.; Kimerling, L.; Hu, J.; Richardson, K.; Agarwal, A.; Tan, D.T.H. On-chip mid-infrared gas detection using chalcogenide glass waveguide. *Appl. Phys. Lett.* **2016**, *108*, 141106. [[CrossRef](#)]
22. Gutierrez-Arroyo, A.; Baudet, E.; Bodiou, L.; Lemaitre, J.; Hardy, I.; Faijan, F.; Bureau, B.; Nazabal, V.; Charrier, J. Optical characterization at 7.7  $\mu\text{m}$  of an integrated platform based on chalcogenide waveguides for sensing applications in the mid-infrared. *Opt. Express* **2016**, *24*, 23109–23117. [[CrossRef](#)] [[PubMed](#)]
23. Lin, H.; Li, L.; Zou, Y.; Danto, S.; Musgraves, J.D.; Richardson, K.; Kozacik, S.; Murakowski, M.; Prather, D.; Lin, P.T.; et al. Demonstration of high-Q mid-infrared chalcogenide glass-on-silicon resonators. *Opt. Lett.* **2013**, *38*, 1470–1472. [[CrossRef](#)] [[PubMed](#)]
24. Yu, M.; Okawachi, Y.; Griffith, A.G.; Picqu e, N.; Lipson, M.; Gaeta, A.L. Silicon-chip-based mid-infrared dual-comb spectroscopy. *Nat. Commun.* **2018**, *9*, 1869. [[CrossRef](#)] [[PubMed](#)]
25. Mashanovich, G.Z.; Milo ević, M.M.; Nedeljkovic, M.; Owens, N.; Xiong, B.; Teo, E.J.; Hu, Y. Low loss silicon waveguides for the mid-infrared. *Opt. Express* **2011**, *19*, 7112–7119. [[CrossRef](#)] [[PubMed](#)]
26. Zou, Y.; Chakravarty, S.; Chen, R.T. Mid-infrared silicon-on-sapphire waveguide coupled photonic crystal microcavities. *Appl. Phys. Lett.* **2015**, *107*, 081109. [[CrossRef](#)]
27. Singh, N.; Hudson, D.D.; Eggleton, B.J. Silicon-on-sapphire pillar waveguides for Mid-IR supercontinuum generation. *Opt. Express* **2015**, *23*, 17345–17354. [[CrossRef](#)] [[PubMed](#)]
28. Lin, P.T.; Singh, V.; Hu, J.; Richardson, K.; Musgraves, J.D.; Luzinov, I.; Hensley, J.; Kimerling, L.C.; Agarwal, A. Chip-scale Mid-Infrared chemical sensors using air-clad pedestal silicon waveguides. *Lab. Chip* **2013**, *13*, 2161–2166. [[CrossRef](#)] [[PubMed](#)]

29. Penadés, J.S.; Ortega-Moñux, A.; Nedeljkovic, M.; Wangüemert-Pérez, J.G.; Halir, R.; Khokhar, A.Z.; Alonso-Ramos, C.; Qu, Z.; Molina-Fernández, I.; Cheben, P.; et al. Suspended silicon mid-infrared waveguide devices with subwavelength grating metamaterial cladding. *Opt. Express* **2016**, *24*, 22908–22916. [[CrossRef](#)] [[PubMed](#)]
30. Penadés, J.S.; Sánchez-Postigo, A.; Nedeljkovic, M.; Ortega-Moñux, A.; Wangüemert-Pérez, J.G.; Xu, Y.; Halir, R.; Qu, Z.; Khokhar, A.Z.; Osman, A.; et al. Suspended silicon waveguides for long-wave infrared wavelengths. *Opt. Lett.* **2018**, *43*, 795–798. [[CrossRef](#)] [[PubMed](#)]
31. Nedeljkovic, M.; Penades, J.S.; Mittal, V.; Murugan, G.S.; Khokhar, A.Z.; Littlejohns, C.; Carpenter, L.G.; Gawith, C.B.; Wilkinson, J.S.; Mashanovich, G.Z. Germanium-on-silicon waveguides operating at mid-infrared wavelengths up to 8.5  $\mu\text{m}$ . *Opt. Express* **2017**, *25*, 27431–27441. [[CrossRef](#)] [[PubMed](#)]
32. Malik, A.; Muneeb, M.; Pathak, S.; Shimura, Y.; Van Campenhout, J.; Loo, R.; Roelkens, G. Germanium-on-silicon mid-infrared arrayed waveguide grating multiplexers. *IEEE Photonics Technol. Lett.* **2013**, *25*, 1805–1808. [[CrossRef](#)]
33. Ramirez, J.M.; Vakarin, V.; Gilles, C.; Frigerio, J.; Ballabio, A.; Chaisakul, P.; Le Roux, X.; Alonso-Ramos, C.; Maisons, G.; Vivien, L.; et al. Low-loss Ge-rich Si 0.2 Ge 0.8 waveguides for mid-infrared photonics. *Opt. Lett.* **2017**, *42*, 105–108. [[CrossRef](#)] [[PubMed](#)]
34. Ramirez, J.M.; Vakarin, V.; Frigerio, J.; Chaisakul, P.; Chrastina, D.; Le Roux, X.; Ballabio, A.; Vivien, L.; Isella, G.; Marris-Morini, D. Ge-rich graded-index Si 1-xGe x waveguides with broadband tight mode confinement and flat anomalous dispersion for nonlinear mid-infrared photonics. *Opt. Express* **2017**, *25*, 6561–6567. [[CrossRef](#)] [[PubMed](#)]
35. Ramirez, J.M.; Liu, Q.; Vakarin, V.; Frigerio, J.; Ballabio, A.; Le Roux, X.; Bouville, D.; Vivien, L.; Isella, G.; Marris-Morini, D. Graded SiGe waveguides with broadband low-loss propagation in the mid infrared. *Opt. Express* **2018**, *26*, 870–877. [[CrossRef](#)] [[PubMed](#)]
36. Vakarin, V.; Ramirez, J.M.; Frigerio, J.; Ballabio, A.; Le Roux, X.; Liu, Q.; Bouville, D.; Vivien, L.; Isella, G.; Marris-Morini, D. Ultra-wideband Ge-rich silicon germanium integrated Mach-Zehnder interferometer for mid-infrared spectroscopy. *Opt. Lett.* **2017**, *42*, 3482–3485. [[CrossRef](#)] [[PubMed](#)]
37. Liu, Q.; Ramirez, J.M.; Vakarin, V.; Le Roux, X.; Ballabio, A.; Frigerio, J.; Chrastina, D.; Isella, G.; Bouville, D.; Vivien, L.; et al. Mid-infrared sensing between 5.2 and 6.6  $\mu\text{m}$  wavelengths using Ge-rich SiGe waveguides. *Opt. Mater. Express* **2018**, *8*, 1305–1312. [[CrossRef](#)]
38. Sinobad, M.; Monat, C.; Luther-Davies, B.; Ma, P.; Madden, S.; Moss, D.J.; Mitchell, A.; Allieux, D.; Orobtschouk, R.; Boutami, S.; et al. Mid-infrared octave spanning supercontinuum generation to 8.5  $\mu\text{m}$  in silicon-germanium waveguides. *Optica* **2018**, *5*, 360–366. [[CrossRef](#)]
39. Carletti, L.; Sinobad, M.; Ma, P.; Yu, Y.; Allieux, D.; Orobtschouk, R.; Brun, M.; Ortiz, S.; Labeye, P.; Nicoletti, S.; et al. Mid-infrared nonlinear optical response of Si-Ge waveguides with ultra-short optical pulses. *Opt. Express* **2015**, *23*, 32202–32214. [[CrossRef](#)] [[PubMed](#)]
40. Serna, S.; Vakarin, V.; Ramirez, J.M.; Frigerio, J.; Ballabio, A.; Roux, X.; Vivien, L.; Isella, G.; Cassan, E.; Dubreuil, N.; et al. Nonlinear Properties of Ge-rich Si 1 – x Ge x Materials with Different Ge Concentrations. *Sci. Rep.* **2017**, *7*, 14692. [[CrossRef](#)] [[PubMed](#)]
41. Soibel, A.; Wright, M.W.; Farr, W.; Keo, S.; Hill, C.; Yang, R.Q.; Liu, H.C. High-speed operation of interband cascade lasers. *Electron. Lett.* **2009**, *45*, 264–265. [[CrossRef](#)]
42. Hinkley, E.D. Laser monitoring of the atmosphere. In *Topics in Applied Physics*; Springer: Berlin, Germany; New York, NY, USA, 1976; Volume 14.
43. Zhang, J.; Ding, S.; Zhai, H.; Dang, A. Theoretical and experimental studies of polarization fluctuations over atmospheric turbulent channels for wireless optical communications. *Opt. Express* **2014**, *22*, 32482–32488. [[CrossRef](#)] [[PubMed](#)]
44. James, D.F. Change of polarization of light beams on propagation in free space. *J. Opt. Soc. Am. A* **1994**, *11*, 1641–1643. [[CrossRef](#)]
45. Pang, X.; Ozolins, O.; Schatz, R.; Storck, J.; Udalcovs, A.; Navarro, J.R.; Kakkar, A.; Maisons, G.; Carras, M.; Jacobsen, G.; et al. Gigabit free-space multi-level signal transmission with a mid-infrared quantum cascade laser operating at room temperature. *Opt. Lett.* **2017**, *42*, 3646–3649. [[CrossRef](#)] [[PubMed](#)]
46. Lumerical Inc. Available online: <http://www.lumerical.com/tcad-products/mode/> (accessed on 28 May 2018).
47. Li, H.H. Refractive index of silicon and germanium and its wavelength and temperature derivatives. *J. Phys. Chem. Ref. Data* **1980**, *9*, 561–658. [[CrossRef](#)]

48. Isella, G.; Chrastina, D.; Rössner, B.; Hackbarth, T.; Herzog, H.J.; König, U.; Von Känel, H. Low-energy plasma-enhanced chemical vapor deposition for strained Si and Ge heterostructures and devices. *Solid-State Electron.* **2004**, *48*, 1317–1323. [[CrossRef](#)]
49. Soref, R. Mid-infrared photonics in silicon and germanium. *Nat. Photonics* **2010**, *4*, 495. [[CrossRef](#)]
50. Thomson, D.J.; Hu, Y.; Reed, G.T.; Fedeli, J.M. Low loss MMI couplers for high performance MZI modulators. *IEEE Photonics Technol. Lett.* **2010**, *22*, 1485–1487. [[CrossRef](#)]
51. Soldano, L.B.; Pennings, E.C.M. Optical multi-mode interference devices based on self-imaging: Principles and applications. *J. Light Technol.* **1995**, *13*, 615–627. [[CrossRef](#)]
52. Bucio, T.D.; Khokhar, A.Z.; Mashanovich, G.Z.; Gardes, F.Y. Athermal silicon nitride angled MMI wavelength division (de) multiplexers for the near-infrared. *Opt. Express* **2017**, *25*, 27310–27320. [[CrossRef](#)] [[PubMed](#)]



© 2018 by the authors. Licensee MDPI, Basel, Switzerland. This article is an open access article distributed under the terms and conditions of the Creative Commons Attribution (CC BY) license (<http://creativecommons.org/licenses/by/4.0/>).